

# Electrical conductivity and crystallization of amorphous bismuth ruthenate thin films deposited by spray pyrolysis

Thomas Ryll,<sup>\*a</sup> Andreas Brunner,<sup>b</sup> Stefan Ellenbroek,<sup>a</sup> Anja Bieberle-Hutter,<sup>a</sup> Jennifer L. M. Rupp<sup>a</sup> and Ludwig J. Gauckler<sup>a</sup>

Received 15th June 2010, Accepted 20th August 2010

DOI: 10.1039/c0cp00889c

Amorphous oxide thin films with tailored functionality will be crucial for the next generation of micro-electro-mechanical-systems (MEMS). Due to potentially favorable electronic and catalytic properties, amorphous bismuth ruthenate thin films might be applied in this regard. We report on the deposition of amorphous bismuth ruthenate thin films by spray pyrolysis, their crystallization behavior and electrical conductivity. At room temperature the 200 nm thin amorphous films exhibit a high electrical conductivity of  $7.7 \times 10^4 \text{ S m}^{-1}$ , which was found to be slightly thermally activated ( $E_a = 4.1 \times 10^{-3} \text{ eV}$ ). It follows that a long-range order of the  $\text{RuO}_6$  octahedra is no precondition for the electrical conductivity of  $\text{Bi}_3\text{Ru}_3\text{O}_{11}$ . Upon heating to the temperature range between 490 °C and 580 °C the initially amorphous films crystallize rapidly. Simultaneously, a transition from a dense and continuous film to isolated  $\text{Bi}_3\text{Ru}_3\text{O}_{11}$  particles on the substrate takes place. Solid-state agglomeration is proposed as the mechanism responsible for disintegration. The area specific resistance of  $\text{Bi}_3\text{Ru}_3\text{O}_{11}$  particles contacted by Pt paste on gadolinia doped ceria electrolyte pellets was found to be  $7 \text{ } \Omega \text{ cm}^2$  at 607 °C in air. Amorphous bismuth ruthenate thin films are proposed for application in electrochemical devices operating at low temperatures, where a high electrical conductivity is required.

## Introduction

Bismuth ruthenate compounds stand out due to a high electronic conductivity<sup>1</sup> and catalytic activity.<sup>2,3</sup> Therefore, crystalline bismuth ruthenate thick films have been considered as thick-film resistors,<sup>4,5</sup> catalysts and electrode materials.<sup>6–15</sup> In the context of cathodes for solid oxide fuel cells (SOFCs) area specific resistances of  $1.6 \text{ } \Omega \text{ cm}^2$  at 700 °C for single-phase  $\text{Bi}_2\text{Ru}_2\text{O}_7$ <sup>9</sup> and  $0.03 \text{ } \Omega \text{ cm}^2$  at 700 °C for a  $\text{Bi}_2\text{Ru}_2\text{O}_7\text{–Bi}_{1.6}\text{Er}_{0.4}\text{O}_3$  composite<sup>11</sup> have been published.

In contrast to bulk samples and thick films no experimental data concerning the processing, phase stability and structural as well as electrical properties of bismuth ruthenate films with thicknesses below one micron are available. Given a potentially high electrical conductivity and catalytic activity, it is of importance to evaluate their usability as electroceramic thin films for micro-electro-mechanical systems (MEMS) such as micro-solid oxide fuel cells ( $\mu$ -SOFCs).<sup>16–18</sup>

Thin film deposition techniques allow for the fabrication of amorphous oxide thin films. Compared to their crystalline counterparts, amorphous thin films feature isotropy, uniformity and fabrication without the need for high temperatures. Hence, amorphous oxide thin films find increasing use in thin-film resistors, photoelectric multilayer devices, solar cells and dielectrics.<sup>19–23</sup> Beyond direct technological application, it is of fundamental interest to study the impact of annealing on the microstructure within multi-phase systems ranging

from amorphous to the biphasic or fully crystalline state during crystallization. Electrical conductivity data for such crystallizing systems are still scarce.

This study aims at the investigation of amorphous bismuth ruthenate thin films deposited by spray pyrolysis. This non-vacuum technique for the deposition of thin films stands out due to low cost, easy upscaling and high deposition rates.<sup>24</sup> The crystallization and microstructural evolution of as-deposited thin films during annealing are discussed and correlated with their electrical properties. As an example of use, the performance of crystallized bismuth ruthenate thin films as SOFC cathodes is evaluated and compared to the literature.

## Structural and electrical properties of bismuth ruthenates

The quasi-binary system  $\text{Bi}_2\text{O}_3\text{–RuO}_2$  contains the two compounds  $\text{Bi}_3\text{Ru}_3\text{O}_{11}$  and  $\text{Bi}_2\text{Ru}_2\text{O}_7$ . According to the phase diagram presented by Hrovat *et al.*,<sup>25</sup> the low-temperature phase  $\text{Bi}_3\text{Ru}_3\text{O}_{11}$  transforms to  $\text{Bi}_2\text{Ru}_2\text{O}_7$  at 950 °C. In this study the denotations “low-temperature phase” and “high-temperature phase” will, therefore, be used for  $\text{Bi}_3\text{Ru}_3\text{O}_{11}$  and  $\text{Bi}_2\text{Ru}_2\text{O}_7$ , respectively. Above 1250 °C  $\text{Bi}_2\text{Ru}_2\text{O}_7$  dissociates into  $\text{Bi}_2\text{O}_3$  and  $\text{RuO}_2$ .

The low-temperature phase  $\text{Bi}_3\text{Ru}_3\text{O}_{11}$  crystallizes in the cubic  $\text{KSbO}_3$  structure.<sup>26</sup> This structure is based on a three-dimensional  $\text{Ru}_{12}\text{O}_{36}$  network comprising pairs of edge sharing  $\text{RuO}_6$  octahedra further connected by corner sharing. The interstitial lattice sites are occupied by an additional  $\text{Bi}_{12}\text{O}_8$  network. The electronic properties of  $\text{Bi}_3\text{Ru}_3\text{O}_{11}$  were mainly studied below room temperature where the

<sup>a</sup> *Nonmetallic Inorganic Materials, Department of Materials, ETH Zurich, Wolfgang-Pauli-Strasse 10, 8093 Zurich, Switzerland. E-mail: thomas.ryll@mat.ethz.ch*

<sup>b</sup> *Institute of Polymers, Department of Materials, ETH Zurich, Wolfgang-Pauli-Strasse 10, 8093 Zurich, Switzerland*

electrical conductivity exhibits a metal-type dependence on temperature.<sup>28–30</sup> The band structure of  $\text{Bi}_3\text{Ru}_3\text{O}_{11}$  is composed of Ru 4d orbitals and oxygen 2p bands close to the Fermi energy.<sup>31</sup> No literature data exist for the electrical conductivity above room-temperature.

The cubic pyrochlore structure of the high-temperature phase  $\text{Bi}_2\text{Ru}_2\text{O}_7$  is specified by the general formula  $[\text{A}_2\text{O}][\text{B}_2\text{O}_6]$ <sup>32</sup> and comprises a three-dimensional network of corner-sharing  $\text{BO}_6$  octahedra interpenetrated by the  $[\text{A}_2\text{O}]$  array. The electrical conductivity of  $\text{Bi}_2\text{Ru}_2\text{O}_7$  exhibits a weak metal-type temperature dependence.<sup>1,33</sup> This can be explained on the basis of the electronic band structure of pyrochlore ruthenates, whose key feature is the splitting of Ru 4d orbitals into  $t_{2g}$  and  $e_g$  states due to the octahedral coordination of the  $\text{Ru}^{4+}$  ions. The Fermi energy  $E_F$  is located at two thirds of the  $t_{2g}$  bands. Their bandwidth is influenced by the Ru–O–Ru angle and Ru–O distance as  $\text{RuO}_6$  octahedra are corner sharing.<sup>34,35</sup> In  $\text{Bi}_2\text{Ru}_2\text{O}_7$  the Ru–O–Ru angles are close to  $133^\circ$  resulting in a bandwidth sufficient for metallic conduction properties. Other pyrochlore ruthenates such as  $\text{Tl}_2\text{Ru}_2\text{O}_7$ <sup>36</sup> exhibit a semiconductor–metal transition while  $\text{Y}_2\text{Ru}_2\text{O}_7$  and  $\text{Gd}_2\text{Ru}_2\text{O}_7$  are semiconductors.<sup>37,38</sup> This is explained by a decreasing size of the A-cation from Bi over Tl to Gd and Y involving a decrease of the Ru–O–Ru angle.<sup>39–41</sup> Further details concerning the structural and electrical properties of  $\text{Bi}_3\text{Ru}_3\text{O}_{11}$  and  $\text{Bi}_2\text{Ru}_2\text{O}_7$  can be found elsewhere.<sup>26,32–35,40,42–44</sup>

Electrical conductivities at room temperature in the range of  $7 \times 10^4 \text{ S m}^{-1}$ <sup>29</sup> to  $1.48 \times 10^5 \text{ S m}^{-1}$ <sup>30</sup> and  $2.5 \times 10^4 \text{ S m}^{-1}$ <sup>40</sup> to  $1.9 \times 10^5 \text{ S m}^{-1}$ <sup>44</sup> were reported for  $\text{Bi}_3\text{Ru}_3\text{O}_{11}$  and  $\text{Bi}_2\text{Ru}_2\text{O}_7$ , respectively. The relatively broad distribution of the conductivity data presumably originates from the dependence of electrical conductivity on the oxygen deficiency of these compounds, which is in turn affected by the oxygen partial pressure during annealing.<sup>44</sup>

## Experimental

### Thin film deposition

Amorphous bismuth ruthenate thin films were deposited by air-pressurized spray pyrolysis on randomly oriented  $\text{Al}_2\text{O}_3$  single crystals and homemade, polycrystalline  $\text{Ce}_{0.8}\text{Gd}_{0.2}\text{O}_{1.9}$  pellets.<sup>27</sup> The composition of the precursor solution as well as detailed parameters used for spray pyrolysis are listed in Table 1. During deposition the precursor solution was pumped (peristaltic pump: Ismatec MS Reglo or syringe pump: Razell Scientific Instruments A99) by means of a viton tube (Masterflex/Cole-Parmer) through a nozzle (Badger

Air-brush Model 150) and atomized by air pressure (pressure regulators: EAR 2000 F 02, SMC and Norgren/IMI). The substrate was centered at a distance of 20 cm below the nozzle on a custom-made heating plate (temperature precision of  $\pm 1^\circ\text{C}$  in the deposition area). More details concerning the spray pyrolysis setup are given elsewhere.<sup>45</sup> Subsequent heat treatments between  $350^\circ\text{C}$  and  $900^\circ\text{C}$  were carried out in air (Nabertherm L3 oven) using a heating and cooling rate of  $3^\circ\text{C min}^{-1}$ .

### Structural and microstructural characterization

A Leo 1530 (Carl Zeiss SMT) scanning electron microscope (SEM) equipped with an energy dispersive X-ray (EDX) detector (Thermo Noran Vantage and Tracor Northern) was used for the characterization of thin films with respect to film thickness, morphology and microstructure. Images were taken by the in-lens detector using an acceleration voltage of 3 kV. For quantitative analysis of grain and pore sizes on the basis of SEM images the software Lince 2.31 was used.<sup>46</sup>

In order to analyze the crystallization and phase transformation behavior of the amorphous film material, differential scanning calorimetry (DSC) and thermogravimetry (TG, both Netzsch STA 449 C Jupiter) were applied. Approximately 20 mg of thin-film material were scratched off from the substrate after ten hours of deposition. The powder was investigated in air using a heating and cooling rate of  $10^\circ\text{C min}^{-1}$  up to a maximum temperature of  $1100^\circ\text{C}$ . Crystallized volume fractions were calculated by integration of the DSC crystallization peak. Further details concerning DSC crystallization experiments on amorphous metal-oxide films deposited by spray pyrolysis can be found elsewhere.<sup>47</sup>

The crystallinity and crystal structure were investigated by X-ray diffraction (Siemens Diffraktometer D5000 Kristalloflex,  $\text{Cu K}_\alpha$  radiation, 40 kV acceleration voltage, 30 mA current) of thin films deposited on  $\text{Al}_2\text{O}_3$  single crystals. For the measurements a step size of  $0.01^\circ$  and a time per step of 12 s were used. Reference peak positions have been calculated by the Inorganic Crystal Structure Database (ICSD) using data obtained by neutron diffraction.<sup>26</sup>

### Electrical and electrochemical characterization

For dc conductivity measurements thin films were deposited through a shadow mask ( $1.4 \text{ cm} \times 2.5 \text{ cm}$  open area, 200  $\mu\text{m}$  thick, laser cut stainless steel) on  $\text{Al}_2\text{O}_3$  single crystals. The films were contacted by stripes of sputtered platinum, platinum paste (Heraeus, C3605 P) and platinum wire. More details are given elsewhere.<sup>48</sup> The wires fixed on the film surface by a ceramic two-component cement

**Table 1** Parameters used for the deposition of bismuth ruthenate thin films by spray pyrolysis

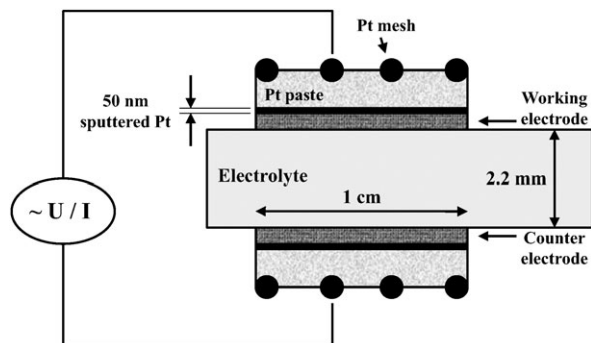
Substrate	$\text{Al}_2\text{O}_3$ single crystals (Stettler, Switzerland, randomly oriented), polycrystalline $\text{Ce}_{0.8}\text{Gd}_{0.2}\text{O}_{1.9}$ pellets <sup>27</sup>
Salt mixture	50 mol% $\text{RuCl}_3 \cdot 3\text{H}_2\text{O}$ (Pressure Chemical, purity $\geq 99.9\%$ ) 50 mol% $\text{BiBr}_3 \cdot 6\text{H}_2\text{O}$ (Aldrich, purity $\geq 98\%$ )
Solvent composition	20 vol% ethanol (Merck, purity $\geq 99.9\%$ , boiling point $78^\circ\text{C}$ ) 80 vol% diethylene glycol monobutyl ether (ABCR, purity 99%, boiling point $231^\circ\text{C}$ )
Total salt concentration	$0.02 \text{ mol l}^{-1}$
Substrate temperature	$280 \pm 5^\circ\text{C}$ , measured with a K type surface probe (Omega Model 88108)
Air pressure	1 bar
Solution flow rate	$30 \text{ ml h}^{-1}$
Spray time	30 min

(Firag Feuerfestkitt) were spot welded (Resistronic 3201) to wires connected to a multimeter (Keithley 2700). During heating and cooling with a rate of  $3\text{ }^{\circ}\text{C min}^{-1}$  a custom made LabView program recorded the four point resistance every 20 s. The maximum temperature given for each sample was maintained for twenty minutes.

Conductivity measurements in air were conducted on a hot plate (Harry Gestigkeit GmbH, CT10), while a closed furnace (Gero) was used for conductivity measurements in pure oxygen and nitrogen (purities: oxygen  $\geq 99.95\text{ vol}\%$ , nitrogen  $\geq 99.995\text{ vol}\%$ , both provided by PanGas). Previous to the measurement the oven was flushed with the corresponding gas for one hour in order to achieve a stable oxygen partial pressure. The flow rates of oxygen and nitrogen were adjusted by manual flow meters to  $60$  and  $200\text{ ml min}^{-1}$ , respectively. For the calculation of error margins of the conductivity data, systematic errors resulting from the uncertainty with respect to sample geometry and thickness as well as statistical errors, which occurred during several measurements of various samples, were taken into account.

Impedance data were measured on symmetrical cells fabricated by the deposition of one square centimetre of thin-film area on both sides of  $\text{Ce}_{0.8}\text{Gd}_{0.2}\text{O}_{1.9}$  (CGO) electrolyte pellets (Scheme 1). For contacting  $50\text{ nm}$  of sputtered platinum (Baltec), platinum paste (Heraeus, C 3605 P) and flattened platinum mesh (52 mesh, woven from  $0.1\text{ mm}$  diameter wire, Johnson Matthey, 99.9%) were used. A detailed description of the electrolyte pellet preparation and the film contacting process is given elsewhere.<sup>27</sup> The thin-film microstructure was adjusted by a heat treatment for 20 min in air at  $600\text{ }^{\circ}\text{C}$ , resulting in a crystallized thin film. The heating and cooling rate was  $3\text{ }^{\circ}\text{C min}^{-1}$ .

Measurements were done in air ( $50\text{ ml min}^{-1}$ ). A type K thermocouple (Omega) touching the substrate was used to monitor the sample temperature. The samples were characterized during cooling in intervals of  $100\text{ }^{\circ}\text{C}$  starting at a maximum temperature of  $600\text{ }^{\circ}\text{C}$ . Previous to the measurements 10 min were awaited isothermally at each temperature step in order to let the sample equilibrate. A Zahner IM6 (Kronach, Germany) impedance analyzer was used for electrochemical impedance spectroscopy (EIS). The frequency interval covered during single measurements ranged from  $0.1\text{ Hz}$  to  $4\text{ MHz}$ , while an amplitude of  $10\text{ mV}$  without dc bias was applied. Impedance



**Scheme 1** Cross-sectional schematic of a symmetrical cell used for the characterization of bismuth ruthenate thin films by electrochemical impedance spectroscopy (EIS).

spectra were analyzed and fitted by an equivalent circuit using the software ZView 2.9c.<sup>49</sup>

## Results and discussion

### Crystallization and microstructure

SEM images of an as-deposited bismuth ruthenate thin film are shown in Fig. 1. The deposition conditions given above resulted in a film thickness of about  $200\text{ nm}$  and a corresponding deposition rate of  $6.7\text{ nm min}^{-1}$  (Fig. 1A). Top-view images (Fig. 1B) revealed that as-deposited thin films were dense, smooth and predominantly crack-free. Some hill-like thickness variations occurred and gave rise to localized crack-formation (Fig. 1C). Such artifacts are characteristic for thin films deposited by droplet deposition techniques.

The crystallization and concurrent microstructural evolution of as-deposited bismuth ruthenate thin films during annealing for 4 h is displayed by XRD patterns and SEM top-view images in Fig. 2 and 3, respectively. A single broad halo was detected in the XRD spectra of samples heat treated at  $400\text{ }^{\circ}\text{C}$ , a temperature  $120\text{ }^{\circ}\text{C}$  higher than the original temperature of deposition (Fig. 2). Hence, the thin films are amorphous after deposition and remain amorphous up to  $400\text{ }^{\circ}\text{C}$ . With respect to microstructure annealing at  $400\text{ }^{\circ}\text{C}$  involved the formation of an irregularly distributed porosity with a mean pore size in the range of  $30\text{ nm}$  (Fig. 3A). In addition, a sporadic growth of  $\text{RuO}_2$  whiskers on the thin film was observed (Fig. 3A). The composition of these crystals, which grew to a length of several microns, was confirmed

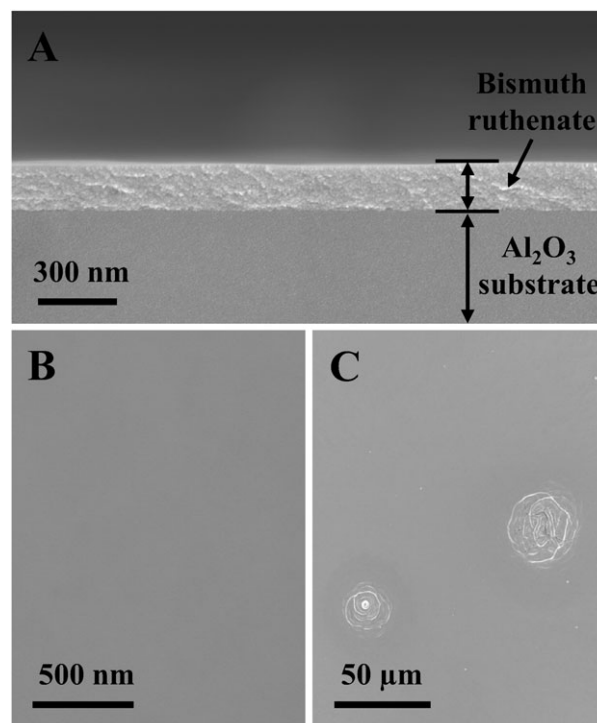


**Fig. 1** SEM images of a bismuth ruthenate thin film as deposited by spray pyrolysis—(A) cross-section, (B) top-view, (C) top-view at low magnification.

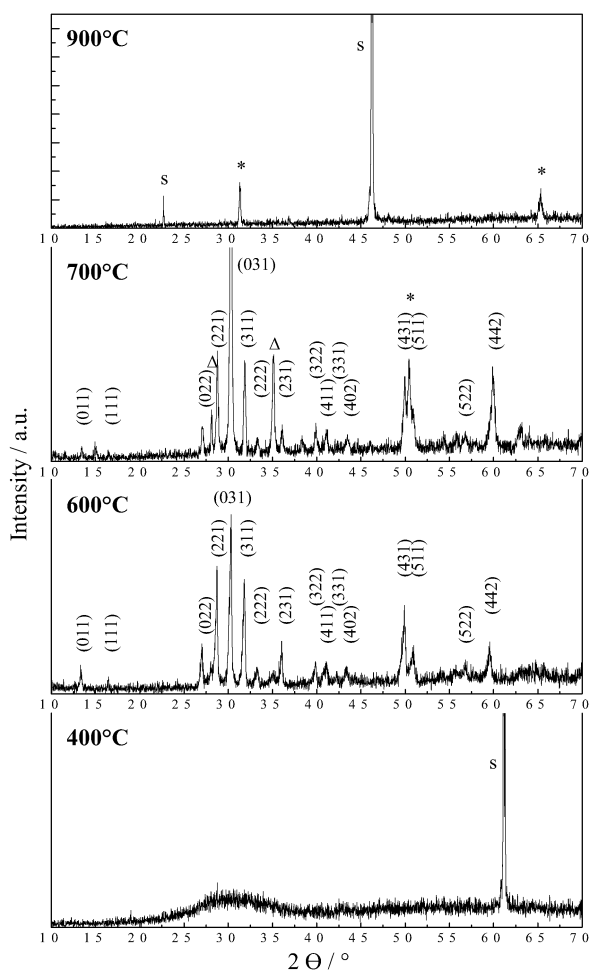


**Fig. 2** XRD patterns of bismuth ruthenate thin films deposited on  $\text{Al}_2\text{O}_3$  single crystals by spray pyrolysis. Samples were heat treated in air for 4 h at different temperatures. Reference peak positions for  $\text{RuO}_2$  ( $\Delta$ ) [JCSF database, 40-1290] are shown. Unassigned reflections (\*) and substrate peaks (s) have been marked.

by EDX measurements. However, their occurrence was too infrequent to be detected by XRD.

Heating of amorphous bismuth ruthenate thin films to 600 °C resulted in crystallized material with distinct XRD peaks (Fig. 2). Refinement of the diffraction pattern by TOPAS (Bruker AXS) as well as comparison with reference data confirmed that  $\text{Bi}_3\text{Ru}_3\text{O}_{11}$  with cubic  $\text{KSbO}_3$  structure formed.<sup>26</sup> The resulting lattice parameter of 9.31 Å corresponded with the literature.<sup>43</sup> SEM images revealed that the  $\text{Bi}_3\text{Ru}_3\text{O}_{11}$  phase formed as crystalline agglomerates with a mean diameter of 900 nm on top of a highly porous structure with a feature size below 40 nm (Fig. 3B). EDX measurements pointed at an equal atomic fraction of bismuth and ruthenium in both the crystalline agglomerates and the porous structure underneath. Therefore, it is assumed that both phases exhibit the same composition. The crystallization of  $\text{Bi}_3\text{Ru}_3\text{O}_{11}$  from material obtained *via* liquid precursors in this temperature range agrees with the work of Linquette-Mailley *et al.*,<sup>12</sup> who prepared  $\text{Bi}_3\text{Ru}_3\text{O}_{11}$  by crystallization (459 °C, 6 h) of material obtained by the pyrosol technique.

After annealing at 700 °C, additional peaks appeared in the XRD spectrum at 28° and 35°  $2\theta$  (Fig. 2, triangles). These were attributed to the formation of  $\text{RuO}_2$  [ICDD database, 40-1290]. The additional peak at approximately 50.5° (star) could not be assigned unambiguously and may refer to an intermediate product. SEM analysis showed that segregated crystalline particles were left behind on the substrate only (Fig. 3C).

Two maxima at 32.5° and 65.5°  $2\theta$  remained in the XRD spectrum besides the substrate signal after a heat treatment at 900 °C. Both could not be assigned to a known bismuth ruthenate phase or one of its end member products. It is assumed that they refer to intermediate bismuth ruthenate products. SEM images revealed no film but isolated crystallites with a size up to several microns on the bare substrate (Fig. 3D).

The DSC heat flux and mass loss of the film material during heating with 10 °C  $\text{min}^{-1}$  are plotted in Fig. 4A. Accordingly, the weight loss between the temperature of deposition and 400 °C added up to 0.52 wt%. As shown in Fig. 3A, samples heat treated at 400 °C in air exhibited an irregularly distributed porosity. Given that the mean density of the solvent composition of 0.92  $\text{g cm}^{-3}$  (value given by the supplier) is approximately ten times lower compared to the density of the crystalline bismuth ruthenate of 9.06  $\text{g cm}^{-3}$  (crystallographic density calculated from XRD data), the volumetric loss in this temperature range can add up to 5%. Hence, the evaporation of organic residues is most likely responsible for the observed formation of porosity.

Starting at 490 °C, the DSC signal exhibits an exothermal peak. Based on the XRD analysis shown in Fig. 2, this exothermal signal is attributed to the evolution of heat during crystallization of the initially amorphous material.<sup>47</sup> In Fig. 4B the crystallized volume fraction is plotted as a function of temperature. The crystallized volume fraction exhibits a sigmoidal curve shape, consistent with the Johnson–Mehl–Avrami kinetics, which is characteristic for the crystallization of metal-oxide glasses.<sup>50</sup> The temperature range around the inflection point of this S-type curve indicates the on-going crystallization and biphasic state of the material. In case of non-isothermal heating full crystallinity of the thin films was obtained at 580 °C, where 99% of the crystallization heat has been released. It is interesting to note that amorphous bismuth ruthenate is characterised by an extremely narrow temperature range of crystallization of roughly 90 °C and exhibits a low temperature required for the activation of nucleation. By contrast, literature reports an up to 6 times larger temperature range for the non-isothermal crystallization of single cation metal oxides such as ceria films and its solid solutions deposited by spray pyrolysis.<sup>47</sup> Similar to the  $\text{SiO}_4$  tetrahedra in silicate glasses the  $\text{RuO}_6$  octahedra have to arrange *via* corner sharing during crystallization and can, in terms of glass-terminology, be considered as the network formers for this material. The  $\text{Bi}_{12}\text{O}_8$  network occupies the interstitials and may act comparable to the network modifier. It is known from the literature that network modifiers reduce the melting point and temperature range of crystallization.<sup>51</sup> Hence, the ability to crystallize faster compared to a one cation oxide such as ceria is reasonable. The rapid nucleation of the material is

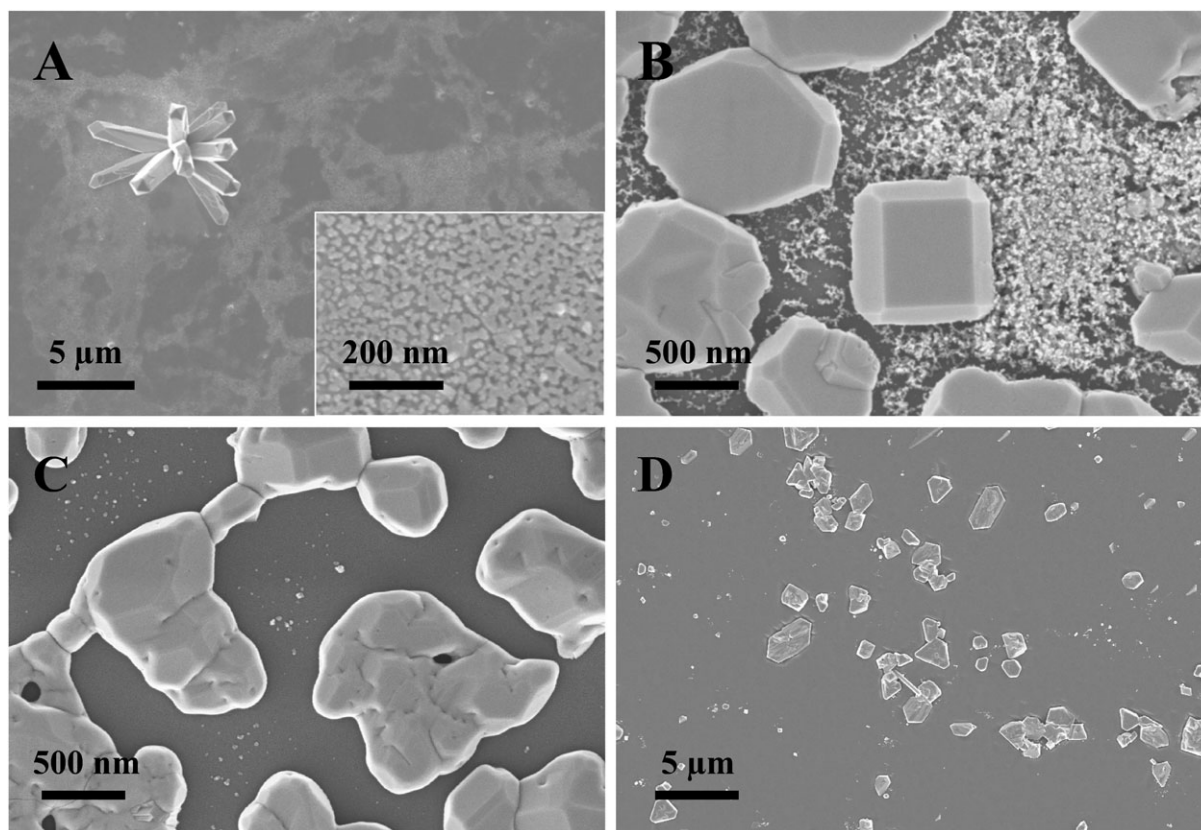


**Fig. 3** SEM top-view images of bismuth ruthenate thin-film microstructures formed during heat treatments for 4 h in air—(A) 400 °C, inset: magnified picture detail, (B) 600 °C, (C) 700 °C, (D) 900 °C.

typical for the processing *via* a wet-chemical precipitation-based thin film route. It was reported in the literature that organic residuals affect the crystallization of metal oxide films and are available as nucleation sites directly after film deposition.<sup>47</sup>

The crystallization in the temperature range between 490 °C and 580 °C was accompanied by an increasing disintegration of the bismuth ruthenate thin films (Fig. 3B). Firstly, it could be argued that the evaporation of organic residues and volatile ruthenium or bismuth compounds gives rise to a mass loss sufficient for film disintegration. This assumption is supported by ruthenium forming the volatile oxide  $\text{RuO}_4$  ( $T_m = 406 \text{ K}$ ),<sup>52</sup> while bismuth is volatile in the metallic state ( $T_m = 544 \text{ K}$ ).<sup>53</sup> Accordingly, the mass loss added up to 3.3 wt% (Fig. 4A) in the temperature range between the temperature of deposition (280 °C) and the end temperature of crystallization (580 °C). However, Beckel *et al.*<sup>48</sup> presented the deposition of  $\text{La}_{0.6}\text{Sr}_{0.4}\text{Co}_{0.2}\text{Fe}_{0.8}\text{O}_{3-\delta}$  (LSCF) thin films by spray pyrolysis using a similar precursor composition (33.3 vol% ethanol, 66.6 vol% diethylene glycol monobutyl ether). In their case the mass loss in the same temperature range was 18 wt% with the LSCF thin films remaining continuous. Hence, the mass loss of 3.3 wt% found in this study is not believed to contain enough film material to cause this enormous change in microstructure on its own. On the other hand, the observed disintegration might be attributed to temperature-facilitated film agglomeration driven by a decrease of interfacial and surface energy. This mechanism is well investigated for metal

and polymer thin films<sup>54–56</sup> and has also been used to explain changes of microstructure during annealing of oxide thin films before.<sup>48</sup> In the temperature range between 580 °C and 700 °C the disintegration of the films ended in separated  $\text{Bi}_3\text{Ru}_3\text{O}_{11}$  islands on the substrate surface (Fig. 3C).

A second feature visible in the DSC signal is a broad endothermic maximum with an onset temperature of 870 °C (Fig. 4A). As thin-film material annealed at 1100 °C for 30 min proved to be  $\text{Bi}_2\text{Ru}_2\text{O}_7$  by XRD (Fig. 5), this endothermic signal is attributed to the phase transformation of  $\text{Bi}_3\text{Ru}_3\text{O}_{11}$  to  $\text{Bi}_2\text{Ru}_2\text{O}_7$ . Although the phase diagram published by Hrovat *et al.*<sup>25</sup> predicts this transformation to happen at 950 °C Gökagac *et al.*<sup>57</sup> observed it at temperatures as low as 750 °C.

It can be concluded that as-deposited bismuth ruthenate thin films are amorphous and dense. Parallel to crystallization in the temperature range between 490 °C and 580 °C a microstructural transition from a continuous thin film to isolated  $\text{Bi}_3\text{Ru}_3\text{O}_{11}$  agglomerates occurs. The detachment of bismuth ruthenate films during annealing at 900 °C is assigned to stress formation during the phase transformation from  $\text{Bi}_3\text{Ru}_3\text{O}_{11}$  to  $\text{Bi}_2\text{Ru}_2\text{O}_7$ , which was found to start at 870 °C.

It is important to note that precipitation-based techniques for the deposition of thin films facilitate the formation of amorphous films and their subsequent investigation in terms of crystallization, phase formation and grain growth. This is particularly interesting in case of multi-phase solid systems.

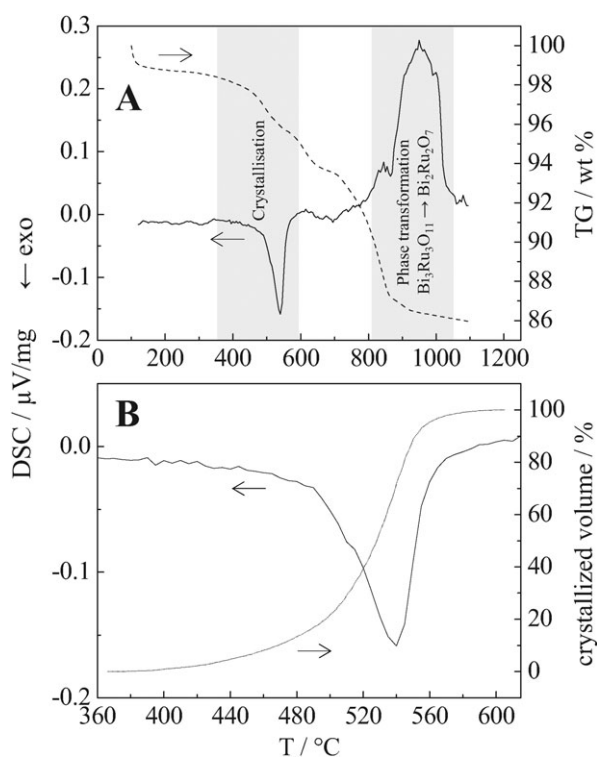


**Fig. 4** (A) DSC and TG results of an as-deposited amorphous bismuth ruthenate film deposited by spray pyrolysis, (B) enlarged view of the evolution of heat during crystallization and the crystallized volume fraction with respect to temperature.

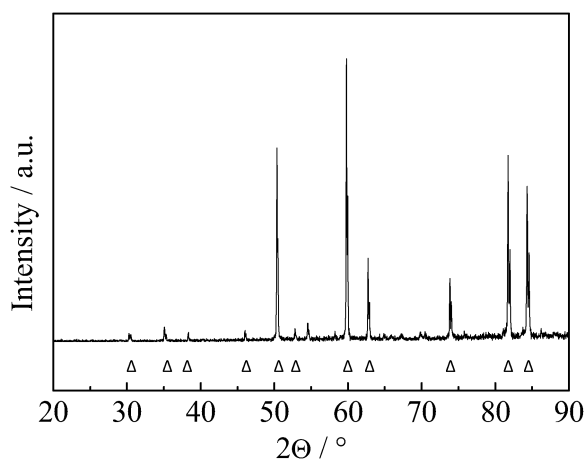


**Fig. 5** XRD pattern of bismuth ruthenate powder. The powder was scraped off from the  $\text{Al}_2\text{O}_3$  substrate after deposition by spray pyrolysis and subsequently annealed for 30 min at  $1100\text{ }^\circ\text{C}$  in air. Reference peak positions for  $\text{Bi}_2\text{Ru}_2\text{O}_7$  ( $\Delta$ ) are shown.<sup>35</sup>

### Electrical conductivity

**Electrical conductivity in the amorphous state.** The electrical conductivity of amorphous bismuth ruthenate thin films was studied during heating cycles between room temperature and  $350\text{ }^\circ\text{C}$  (Fig. 6). This temperature range was chosen on the basis of the XRD and DSC analysis with the objective of maintaining an amorphous microstructure.

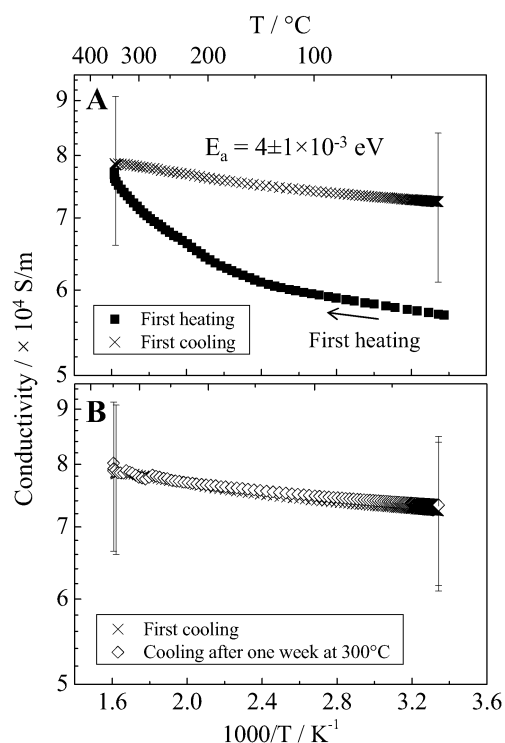


**Fig. 6** Electrical conductivity of amorphous bismuth ruthenate films deposited at  $350\text{ }^\circ\text{C}$  on  $\text{Al}_2\text{O}_3$  single crystals and not heated beyond the crystallization temperature—(A) conductivity measured in air during the first heating and cooling cycle after deposition. (B) Comparison of conductivities measured during cooling before and after a heat treatment for one week at  $300\text{ }^\circ\text{C}$ . The activation energy for the electrical conductivity between room temperature and  $300\text{ }^\circ\text{C}$  measured during cooling is also shown.

During the first heating from room temperature to  $350\text{ }^\circ\text{C}$  the electrical conductivity increased (Fig. 6A). Subsequent cooling as well as additional heating cycles revealed a reproducible and slightly thermally activated conductivity. Assuming an Arrhenius-type thermal activation an activation energy of  $4 \pm 1 \times 10^{-3}\text{ eV}$  was determined. The standard deviation given for this value is based upon the statistical error of fourteen measurements on four samples. Interestingly, an electrical conductivity approximately 30% higher compared to the initial value of as-deposited films remained in the amorphous thin films once the first heating was accomplished. This could be related to chemical or structural changes in the short range order of the amorphous bismuth ruthenate due to evaporation of organic residues.

The stability of electrical conductivity featured by the amorphous films was evaluated by subjecting a sample to one week of isothermal dwell at  $300\text{ }^\circ\text{C}$ . The conductivity of this film measured during cooling and a sample cooled after the initial heating without isothermal dwell are compared in Fig. 6B. The comparison revealed that the electrical conductivity of amorphous bismuth ruthenate thin films remains stable for at least one week.

The mean electrical conductivity of amorphous bismuth ruthenate thin films heated to  $350\text{ }^\circ\text{C}$  is compared to literature data for crystalline samples of bulk  $\text{Bi}_3\text{Ru}_3\text{O}_{11}$  and  $\text{Bi}_2\text{Ru}_2\text{O}_7$  in Table 2. Accordingly, the electrical conductivity of the

**Table 2** Conductivity data of bismuth ruthenate samples

Compound	Electrical conductivity/S m <sup>-1</sup> at		Sample	Source
	25 °C	500 °C		
Amorphous Bi <sub>3</sub> Ru <sub>3</sub> O <sub>11</sub>	(7.7±7) × 10 <sup>4</sup>	—	Thin film	This study
	7 × 10 <sup>4</sup>	—	Bulk	29
	1.48 × 10 <sup>5</sup>	—	Bulk	30
Bi <sub>2</sub> Ru <sub>2</sub> O <sub>7</sub>	1.33 × 10 <sup>5</sup>	9.4 × 10 <sup>4</sup>	Bulk	1
	2.5 × 10 <sup>4</sup>	—	Bulk	40
	—	1.66 × 10 <sup>5</sup>	Bulk	33
	1.9 × 10 <sup>5</sup>	—	Bulk	44

amorphous bismuth ruthenate thin films complies with the conductivity of the low-temperature phase Bi<sub>3</sub>Ru<sub>3</sub>O<sub>11</sub> reported by Fujita *et al.*<sup>29</sup> This reveals that a long range order of the RuO<sub>6</sub> octahedra is no precondition for the magnitude of electrical conductivity featured by this compound. However, a slightly thermally activated conductivity ( $E_a = 4 \pm 1 \times 10^{-3}$  eV) was observed in contrast to crystalline Bi<sub>3</sub>Ru<sub>3</sub>O<sub>11</sub> and Bi<sub>2</sub>Ru<sub>2</sub>O<sub>7</sub> which are metal-type conductors.<sup>1,29,30,33</sup> This subtle metal–semiconductor transition, going from crystalline Bi<sub>3</sub>Ru<sub>3</sub>O<sub>11</sub> to an amorphous thin film, might trace back to a changed Ru–O–Ru angle in the near ordered glassy state compared to the long-range ordered KSbO<sub>3</sub> structure of Bi<sub>3</sub>Ru<sub>3</sub>O<sub>11</sub>, resulting in a decreased density of states at the Fermi level. Analogously, a reduction of the Ru–O–Ru angle resulting from a decreasing size of the A-side cation has been used before in order to interpret metal-semiconductor transitions in crystalline pyrochlore ruthenates.<sup>40,41</sup> Even though the energy bands in glassy oxides can no longer be considered quasicontinuous, their calculation is still feasible on the basis of near ordered clusters leading to similar results.<sup>22,58</sup>

In order to shed additional light on the mechanism of electrical conduction in amorphous bismuth ruthenate thin films, the impact of oxygen partial pressure and different gas atmospheres on the electrical conductivity was investigated by conductivity measurements in oxygen, air and nitrogen up to a maximum temperature of 320 °C. In Fig. 7 the measured conductivities are plotted as a function of oxygen partial pressure for three different temperatures. The conductivity did not change in the oxygen partial pressure range between 1 and 10<sup>5</sup> Pa corresponding to the gas atmospheres of nitrogen

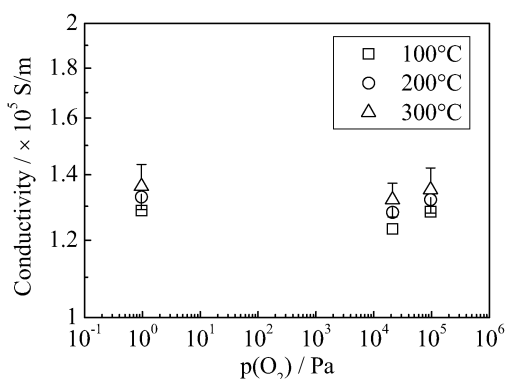


**Fig. 7** Dependence of the electrical conductivity of amorphous bismuth ruthenate films deposited on Al<sub>2</sub>O<sub>3</sub> single crystals on oxygen partial pressure. For clarity error bars are shown for conductivities measured at 300 °C down to an oxygen partial pressure of 1 Pa.

and oxygen, respectively. This agrees with literature data for crystalline Bi<sub>2</sub>Ru<sub>2</sub>O<sub>7</sub> where a substantial drop of electrical conductivity with decreasing oxygen partial pressure was observed above 700 °C only.<sup>59</sup> Therefore, reactions of the amorphous film with the gas atmospheres oxygen, air and nitrogen at a maximum temperature of 320 °C can be excluded.

**Electrical conductivity during crystallization.** The electrical conductivity of as-deposited thin films measured during three subsequent heating cycles with  $\pm 3$  °C min<sup>-1</sup> in air is plotted in Fig. 8. The electrical data will be discussed in view of the microstructural changes during crystallization shown in Fig. 9.

During the first heating of the amorphous thin film, the electrical conductivity increased from  $5.9 \times 10^4$  S m<sup>-1</sup> at room temperature to  $9.1 \times 10^4$  S m<sup>-1</sup> at 409 °C. As mentioned before, this increase during the first heating supposedly originates from chemical or structural changes in the short-range order of the amorphous bismuth ruthenate.

The corresponding microstructure at 400 °C is shown in Fig. 9A. The amorphous films were continuous and exhibited an irregularly distributed porosity with a pore size in the range of 30 nm.

The maximum of electrical conductivity at 409 °C was followed by a decrease during further heating resulting in an electrical conductivity of  $3.0 \times 10^4$  S m<sup>-1</sup> at room temperature at the end of the first heating cycle. Previous DSC experiments revealed a start temperature of crystallization of 490 °C, which is 81 °C higher than the observed maximum of conductivity. The reason for the difference is the gradual start of crystallization (compare Fig. 4). While it was the onset of the crystallization peak which was used to define the start temperature of crystallization, it might well be that some crystallization does already take place at lower temperatures. Hence, the drop in electrical conductivity can be attributed to the beginning crystallization and concurrent disintegration of the thin films.

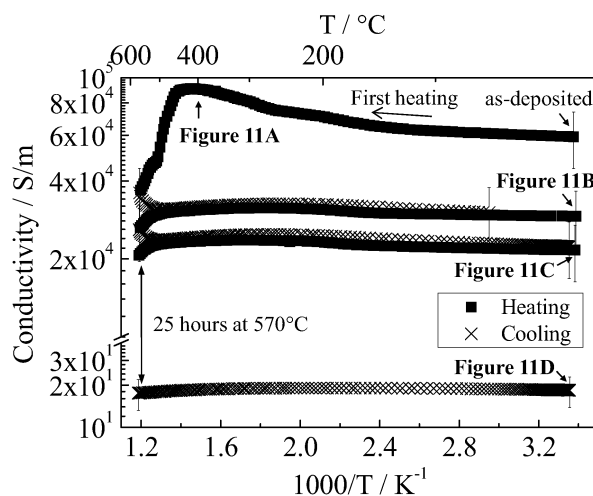


**Fig. 8** Electrical conductivity of an initially amorphous bismuth ruthenate film deposited on a Al<sub>2</sub>O<sub>3</sub> single crystal. Conductivity was measured in air during three subsequent heating and cooling cycles, interrupted by isothermal annealing for 25 hours at 570 °C. Characters refer to the corresponding microstructures shown in Fig. 9.

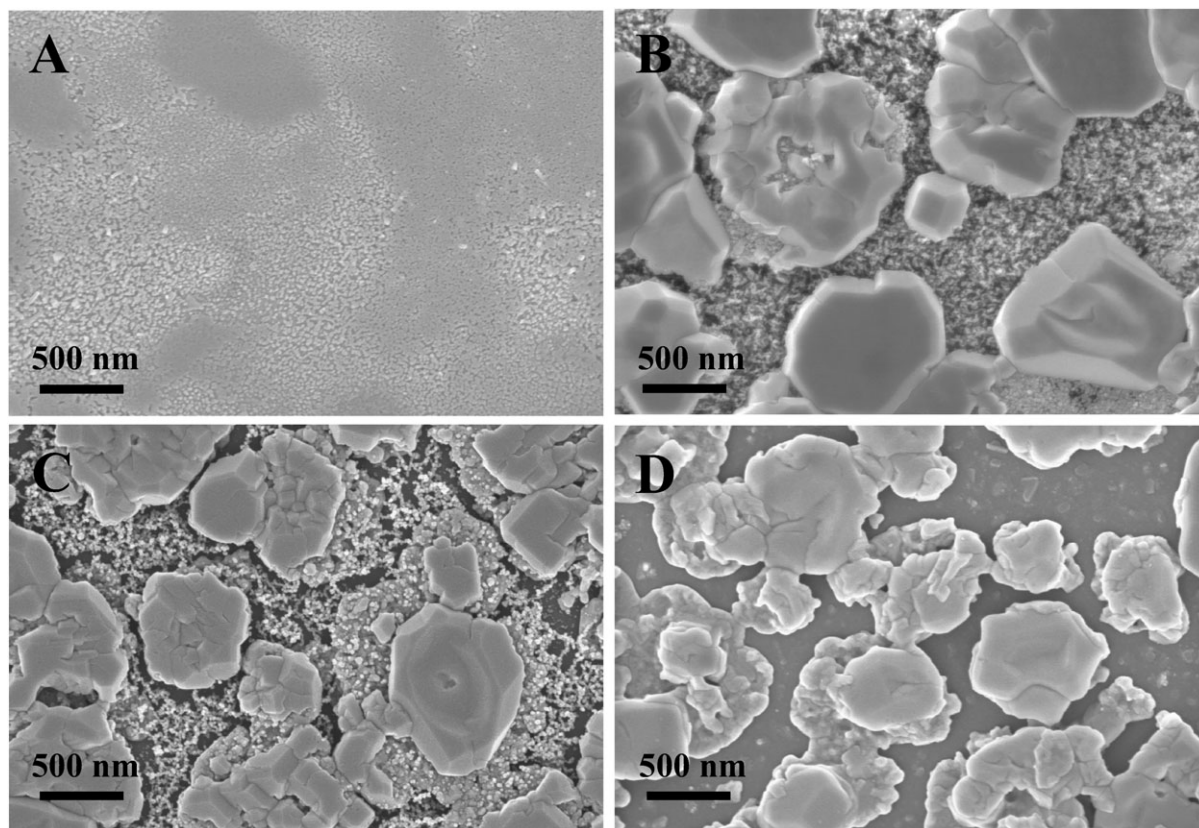


**Fig. 9** SEM top-view images of bismuth ruthenate thin-film microstructures formed during conductivity measurements in air—(A) heated to 400 °C, (B) 20 min at 580 °C, (C) 40 min at 580 °C, (D) 25 h at 570 °C.

A steady decrease of the electrical conductivity was observed during further heating cycles. Microstructural analysis revealed a proceeding agglomeration of  $\text{Bi}_3\text{Ru}_3\text{O}_{11}$  crystals on the film surface as well as an increasing porosity (Fig. 9B and C). After isothermal annealing for 25 h at 570 °C during the third heating cycle a complete breakdown of conductivity over three orders of magnitude was observed. This was caused by a loss of percolation during the isothermal hold resulting in completely segregated  $\text{Bi}_3\text{Ru}_3\text{O}_{11}$  agglomerates (Fig. 9D).

Summarizing, it can be stated that the electrical conductivity of amorphous bismuth ruthenate thin films complies with their crystalline counterpart  $\text{Bi}_3\text{Ru}_3\text{O}_{11}$ . In contrast, the temperature dependence changed from metallic to semiconducting. A dependence of the electrical conductivity on the oxygen partial pressure was not observed. This indicates that at 300 °C the oxygen non-stoichiometry does not change in the oxygen partial pressure range between pure nitrogen and oxygen. The disintegration of the thin films during crystallization involves a breakdown of the electrical in-plane conductivity due to a loss of percolation.

#### Area specific resistance (ASR) of $\text{Bi}_3\text{Ru}_3\text{O}_{11}$ particles

The performance of SOFC cathodes is typically specified by means of the area specific resistance (ASR). The ASR is calculated by multiplying the cathode polarization resistance by the cathode area. In this study electrochemical impedance

spectroscopy (EIS) was used to determine the ASR of crystalline and agglomerated bismuth ruthenate thin films. In this regard symmetrical cells with bismuth ruthenate electrode films on sintered CGO electrolyte pellets were fabricated (Scheme 1). Amorphous bismuth ruthenate thin films could not be characterized by means of their ASR, as the electrode response at temperatures lower than 350 °C occurred beneath the lower end of the frequency range covered in this study (0.1 Hz).

$\text{Bi}_3\text{Ru}_3\text{O}_{11}$  particles contacted by Pt paste were characterized by EIS between 404 °C and 607 °C. The resulting spectra contained two arcs and were fitted by the equivalent circuit shown in Fig. 10. The high-frequency arc was attributed to the CGO electrolyte since the conductivity and the activation energy of 0.98 eV were comparable to literature data for CGO.<sup>60–62</sup> In addition, the high-frequency arc was identical for amorphous and crystalline bismuth ruthenate electrodes.

The low-frequency arc in the spectra was assigned to the cathode process as the summit frequency of the low-frequency arc corresponded to values reported in the literature for the electrode processes.<sup>27,63,64</sup> In order to verify that the  $\text{Bi}_3\text{Ru}_3\text{O}_{11}$  particles on the CGO surface indeed had an effect on the ASR of the platinum current collector, a third sample composed of the electrolyte and the platinum current collector only was measured. It was found that the polarization resistance of the current collector was approximately one order of magnitude larger compared to the polarization resistance measured in the presence of the crystalline  $\text{Bi}_3\text{Ru}_3\text{O}_{11}$

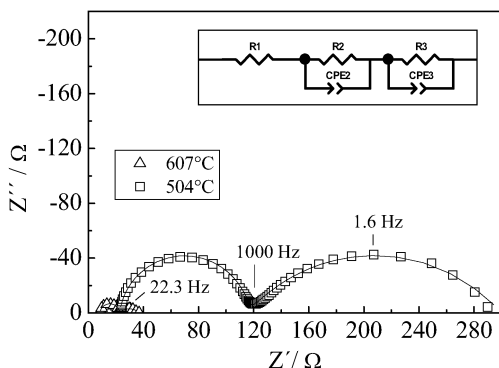


**Fig. 10** Impedance spectra of crystalline  $\text{Bi}_3\text{Ru}_3\text{O}_{11}$  particles on  $\text{Ce}_{0.8}\text{Gd}_{0.2}\text{O}_{1.9}$  measured at 504 °C and 607 °C. Prior to the measurement the sample was heat treated at 600 °C for 4 hours. The continuous line corresponds to impedance spectra obtained by the adaption of an equivalent circuit to the measured data. The used equivalent circuit is shown in the inset. R: ohmic resistance, CPE: constant phase element.

particles. As the electrodes on both sides of the electrolyte pellet were prepared identically, only half the polarization resistance was attributed to one electrode.

The ASR of the  $\text{Bi}_3\text{Ru}_3\text{O}_{11}$  particles is shown in Fig. 11. Assuming an Arrhenius type thermal activation an activation energy of 1.17 eV was calculated. For comparison literature data for  $\text{Bi}_2\text{Ru}_2\text{O}_7$  thick films<sup>9,12</sup> and a state-of-the-art  $\text{La}_{0.6}\text{Sr}_{0.4}\text{Co}_{0.2}\text{Fe}_{0.8}\text{O}_{3-\delta}$  (LSCF) thin film, deposited by spray pyrolysis on CGO,<sup>27</sup> are shown as well. No literature data are available for the ASR of  $\text{Bi}_3\text{Ru}_3\text{O}_{11}$ . Comparison with the literature reveals that (i) the fully crystalline  $\text{Bi}_3\text{Ru}_3\text{O}_{11}$  particles, processed by spray pyrolysis in this study, show a comparable absolute ASR as well as activation energy compared to the electrically better conducting  $\text{Bi}_2\text{Ru}_2\text{O}_7$  phase and (ii) at 500 °C the fully crystalline  $\text{Bi}_3\text{Ru}_3\text{O}_{11}$  film deposited by spray pyrolysis shows an ASR half an order of magnitude larger compared to the state-of-the-art SOFC cathode material LSCF. However, the loss of in-plane conductivity during annealing is detrimental since it necessitates contacting from above. Due to their low activation energy of 1.17 eV compared to state-of-the-art cathode materials like LSCF ( $E_a = 1.55$  eV),<sup>27</sup>  $\text{Bi}_3\text{Ru}_3\text{O}_{11}$  thin films are a promising

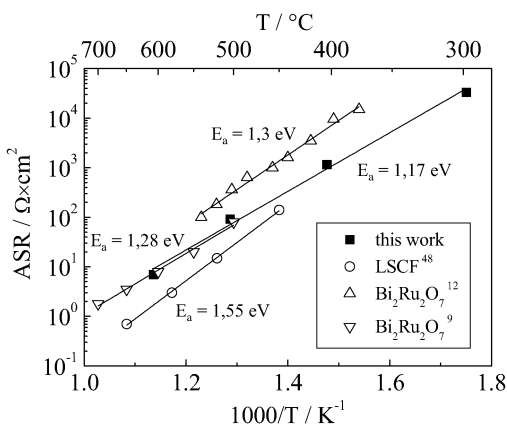


**Fig. 11** ASR of crystalline  $\text{Bi}_3\text{Ru}_3\text{O}_{11}$  particles on  $\text{Ce}_{0.8}\text{Gd}_{0.2}\text{O}_{1.9}$ . For comparison literature data for  $\text{Bi}_2\text{Ru}_2\text{O}_7$  thick films<sup>9,12</sup> and a  $\text{La}_{0.6}\text{Sr}_{0.4}\text{Co}_{0.2}\text{Fe}_{0.8}\text{O}_{3-\delta}$  (LSCF) thin film<sup>27</sup> is shown.

cathode for low-temperature applications, *i.e.* micro-SOFCs operating below 400 °C.<sup>16,65</sup>

## Conclusions

Amorphous bismuth ruthenate thin films deposited at 350 °C exhibit a high electrical conductivity of  $7.7 \times 10^4 \text{ S m}^{-1}$  at room temperature. This value is comparable with literature data for crystalline  $\text{Bi}_3\text{Ru}_3\text{O}_{11}$  bulk samples and stable for at least one week at 300 °C in air. We conclude that a long-range order of the  $\text{RuO}_6$  octahedra is no precondition for the electrical conductivity of  $\text{Bi}_3\text{Ru}_3\text{O}_{11}$ . In contrast to crystalline  $\text{Bi}_3\text{Ru}_3\text{O}_{11}$ , the electrical conductivity of amorphous bismuth ruthenate thin films is slightly thermally activated with an activation energy of  $E_a = 4 \pm 1 \times 10^{-3} \text{ eV}$ . This might trace back to a different Ru–O–Ru angle in the amorphous compared to the crystalline state. Potential application areas for amorphous bismuth ruthenate thin films are conductive thin-film structures in electronic devices or thin-film electrodes where an amorphous microstructure is required.

Amorphous bismuth ruthenate thin films crystallize between 490 °C and 580 °C. This temperature range is surprisingly narrow compared to other precipitation-based metal oxide thin films like ceria and its solid solutions. Glass terminology allotting the role of the network former to the  $\text{RuO}_6$  octahedra and the function of a network modifier to the  $\text{Bi}_{12}\text{O}_8$  network was applied to explain this behavior.

Crystallization involves a disintegration of bismuth ruthenate thin films into crystalline  $\text{Bi}_3\text{Ru}_3\text{O}_{11}$  agglomerates with cubic  $\text{KSbO}_3$  structure. The disintegration is accompanied by a loss of percolation, resulting in a stepwise breakdown of the electrical sheet-conductivity. Given the comparatively moderate mass loss of 3.3% during crystallization the disintegration is ascribed to a temperature-driven agglomeration process in combination with the evaporation of thin film material. Upon further heating to 900 °C the phase transformation to the pyrochlore  $\text{Bi}_2\text{Ru}_2\text{O}_7$  at 870 °C results in delamination of the agglomerates from the substrate.

$\text{Bi}_3\text{Ru}_3\text{O}_{11}$  particles contacted by Pt paste have been evaluated with respect to their area specific resistance (ASR) as solid oxide fuel cell (SOFC) cathodes on CGO electrolyte pellets. The ASR of  $7 \text{ } \Omega \text{ cm}^2$  at 600 °C is consistent with literature data for  $\text{Bi}_2\text{Ru}_2\text{O}_7$  thick films. Due to a low activation energy of 1.17 eV between 400 °C and 600 °C  $\text{Bi}_3\text{Ru}_3\text{O}_{11}$  based cathodes are promising for SOFCs operating at low temperatures.

## Acknowledgements

The authors like to thank Prof. Joop Schoonman of the Delft University of Technology for advice and helpful discussions. Furthermore, financial support by the following Swiss institutions is gratefully acknowledged:

- Competence Centre for Materials Science and Technology (CCMX), Switzerland, within the framework of the project NANCER
- Center of Competence Energy and Mobility (CEEM)
- Swiss Electric Research (SER)

## Notes and references

- 1 R. J. Bouchard and J. L. Gillson, *Mater. Res. Bull.*, 1971, **6**, 669.
- 2 H. S. Horowitz, J. M. Longo and H. H. Horowitz, *J. Electrochem. Soc.*, 1983, **130**, 1851.
- 3 R. G. Egdell, J. B. Goodenough, A. Hamnett and C. C. Naish, *J. Chem. Soc., Faraday Trans. 1*, 1983, **79**, 893.
- 4 P. F. Carcia, A. Ferretti and A. Suna, *J. Appl. Phys.*, 1982, **53**, 5282.
- 5 B. Morten, A. Masoero, M. Prudenziati and T. Manfredini, *J. Phys. D: Appl. Phys.*, 1994, **27**, 2227.
- 6 T. Takeda, R. Kanno, Y. Kawamoto, Y. Takeda and O. Yamamoto, *J. Electrochem. Soc.*, 2000, **147**, 1730.
- 7 J. S. Ahn, D. Pergolesi, M. A. Camaratta, H. Yoon, B. W. Lee, K. T. Lee, D. W. Jung, E. Traversa and E. D. Wachsman, *Electrochem. Commun.*, 2009, **11**, 1504.
- 8 A. Jaiswal and E. D. Wachsman, *J. Electrochem. Soc.*, 2005, **152**, A787.
- 9 A. Jaiswal, C. T. Hu and E. D. Wachsman, *J. Electrochem. Soc.*, 2007, **154**, B1088.
- 10 A. Jaiswal and E. Wachsman, *Ionics*, 2009, **15**, 1.
- 11 M. Camaratta and E. Wachsman, *J. Electrochem. Soc.*, 2008, **155**, B135.
- 12 S. Linquette-Mailley, A. Caneiro, E. Djurado, G. Mairesse and J. Foulletier, *Solid State Ionics*, 1998, **107**, 191.
- 13 Z. M. Zhong, *Electrochem. Solid-State Lett.*, 2006, **9**, A215.
- 14 V. Esposito, B. H. Luong, E. Di Bartolomeo, E. D. Wachsman and E. Traversa, *J. Electrochem. Soc.*, 2006, **153**, A2232.
- 15 J. M. Bae and B. C. H. Steele, *J. Electroceram.*, 1999, **3**, 37.
- 16 A. Bieberle-Hutter, D. Beckel, A. Infortuna, U. P. Muecke, J. L. M. Rupp, L. J. Gauckler, S. Rey-Mermet, P. Muralt, N. R. Bieri, N. Hotz, M. J. Stutz, D. Poulikakos, P. Heeb, P. Muller, A. Bernard, R. Gmur and T. Hocker, *J. Power Sources*, 2008, **177**, 123.
- 17 U. P. Muecke, D. Beckel, A. Bernard, A. Bieberle-Hutter, S. Graf, A. Infortuna, P. Muller, J. L. M. Rupp, J. Schneider and L. J. Gauckler, *Adv. Funct. Mater.*, 2008, **18**, 3158.
- 18 A. Evans, A. Bieberle-Hütter, J. L. M. Rupp and L. J. Gauckler, *J. Power Sources*, 2009, **194**, 119.
- 19 E. M. C. Fortunato, P. M. C. Barquinha, A. Pimentel, A. M. F. Goncalves, A. J. S. Marques, L. M. N. Pereira and R. F. P. Martins, *Adv. Mater.*, 2005, **17**, 590.
- 20 S. R. Das, *Thin Solid Films*, 1984, **119**, 31.
- 21 T. Tsukada, *J. Non-Cryst. Solids*, 1993, **166**, 721.
- 22 R. Grigorovici, *Thin Solid Films*, 1972, **9**, 1.
- 23 R. Grigorovici, *Thin Solid Films*, 1972, **12**, 153.
- 24 P. S. Patil, *Mater. Chem. Phys.*, 1999, **59**, 185.
- 25 M. Hrovat, S. Bernik and D. Kolar, *J. Mater. Sci. Lett.*, 1988, **7**, 637.
- 26 F. Abraham, D. Thomas and G. Nowogrocki, *Bull. Soc. Fr. Mineral. Cristallogr.*, 1975, **98**, 25.
- 27 D. Beckel, U. P. Muecke, T. Gyger, G. Florey, A. Infortuna and L. J. Gauckler, *Solid State Ionics*, 2007, **178**, 407.
- 28 K. Tsuchida, C. Kato, T. Fujita, Y. Kobayashi and M. Sato, *J. Phys. Soc. Jpn.*, 2004, **73**, 698.
- 29 T. Fujita, K. Tsuchida, Y. Yasui, Y. Kobayashi and M. Sato, *Physica B (Amsterdam)*, 2003, **329–333**, 743.
- 30 W. L. Lee, M. K. Haas, G. Lawes, A. P. Ramirez, R. J. Cava and N. P. Ong, *Europhys. Lett.*, 2003, **63**, 860.
- 31 L. He, J. R. Anderson, H. F. Franzen and D. C. Johnson, *Chem. Mater.*, 1997, **9**, 715.
- 32 F. Abraham, G. Nowogrocki and D. Thomas, *C. R. Acad. Sci., Ser. IIc Chim.*, 1975, **280**, 279.
- 33 M. Yasukawa, S. Kuniyoshi and T. Kono, *Solid State Commun.*, 2003, **126**, 213.
- 34 F. Ishii and T. Oguchi, *J. Phys. Soc. Jpn.*, 2000, **69**, 526.
- 35 M. Avdeev, M. K. Haas, J. D. Jorgenson and R. J. Cava, *J. Solid State Chem.*, 2002, **169**, 24.
- 36 A. W. Sleight and J. L. Gillson, *Mater. Res. Bull.*, 1971, **6**, 781.
- 37 R. Aleonard, E. F. Bertaut, M. C. Montmory and R. Pauthenet, *J. Appl. Phys.*, 1962, **33**, 1205.
- 38 M. A. Subramanian, G. Aravamudan and G. V. S. Rao, *Prog. Solid State Chem.*, 1983, **15**, 55.
- 39 P. A. Cox, J. B. Goodenough, P. J. Tavener, D. Telles and R. G. Egdell, *J. Solid State Chem.*, 1986, **62**, 360.
- 40 R. Kanno, Y. Takeda, T. Yamamoto, Y. Kawamoto and O. Yamamoto, *J. Solid State Chem.*, 1993, **102**, 106.
- 41 K. S. Lee, D. K. Seo and M. H. Whangbo, *J. Solid State Chem.*, 1997, **131**, 405.
- 42 S. Yoshii and M. Sato, *J. Phys. Soc. Jpn.*, 1999, **68**, 3034.
- 43 G. R. Facer, M. M. Elcombe and B. J. Kennedy, *Aust. J. Chem.*, 1993, **46**, 1897.
- 44 R. E. Carbonio, J. A. Alonso and J. L. Martinez, *J. Phys.: Condens. Matter*, 1999, **11**, 361.
- 45 D. Beckel, A. Dubach, A. R. Studart and L. J. Gauckler, *J. Electroceram.*, 2006, **16**, 221.
- 46 S. L. dos Santos e Lucato, *Lince 2.31*, Department of Materials Science, Darmstadt University of Technology, Darmstadt, Germany, 1999.
- 47 J. L. M. Rupp, B. Scherrer, A. Harvey and L. J. Gauckler, *Adv. Funct. Mater.*, 2009, **19**, 9.
- 48 D. Beckel, A. Dubach, A. N. Grundy, A. Infortuna and L. J. Gauckler, *J. Eur. Ceram. Soc.*, 2008, **28**, 49.
- 49 D. Johnson, *ZView 2.9c*, Scribner Associates, Inc, 2005.
- 50 K. A. Jackson, *Nucleation, Kinetic Processes*, Wiley-VCH Verlag GmbH & Co., ch. 15, 2004.
- 51 I. Gutzow and J. Schmelzer, *The Vitreous State: Thermodynamics, Structure, Rheology and Crystallization*, Springer-Verlag, 1995.
- 52 J. A. Rard, *Chem. Rev.*, 1985, **85**, 1.
- 53 C. R. Hammond, *Handbook of Chemistry and Physics*, CRC press, 81st edn, 2004.
- 54 U. Thiele, M. Mertig and W. Pompe, *Phys. Rev. Lett.*, 1998, **80**, 2869.
- 55 R. Saxena, M. J. Frederick, G. Ramanath, W. N. Gill and J. L. Plawsky, *Phys. Rev. B: Condens. Matter Mater. Phys.*, 2005, **72**, 115425.
- 56 D. J. Srolovitz and M. G. Goldiner, *JOM—J. Miner. Met. Mater. Soc.*, 1995, **47**, 31.
- 57 G. Gökagac and B. J. Kennedy, *Langmuir*, 1993, **9**, 1862.
- 58 R. E. Hummel, *Electronic Properties of Materials*, Springer, 2001.
- 59 B. Rehak, M. Frumar and L. Koudelka, *J. Mater. Sci. Lett.*, 1984, **3**, 1011.
- 60 V. V. Kharton, F. M. Figueiredo, L. Navarro, E. N. Naumovich, A. V. Kovalevsky, A. A. Yaremchenko, A. P. Viskup, A. Carneiro, F. M. B. Marques and J. R. Frade, *J. Mater. Sci.*, 2001, **36**, 1105.
- 61 T. S. Zhang, J. Ma, S. H. Chan, P. Hing and J. A. Kilner, *Solid State Sci.*, 2004, **6**, 565.
- 62 A. Jasper, J. A. Kilner and D. W. McComb, *Solid State Ionics*, 2008, **179**, 904.
- 63 W. G. Wang and M. Mogensen, *Solid State Ionics*, 2005, **176**, 457.
- 64 V. Dusastre and J. A. Kilner, *Solid State Ionics*, 1999, **126**, 163.
- 65 H. Huang, M. Nakamura, P. Su, R. Fasching, Y. Saito and F. B. Prinz, *J. Electrochem. Soc.*, 2007, **154**, B20.